Effects of fluid rheology and pore connectivity on rock permeability based on a network model

Fansheng Xiong[1,2], **Weitao Sun**[1,2*], **Jing Ba**[3†] **and José M. Carcione**[3, 4]

[1] School of Aerospace Engineering, Tsinghua University, Beijing 100084, China

[2] Zhou Pei-Yuan Center for Applied Mathematics, Tsinghua University, Beijing 100084, China

[3] School of Earth Sciences and Engineering, Hohai University, Nanjing, 211100, China

[4] Istituto Nazionale di Oceanografia e di Geofisica Sperimentale (OGS), Borgo Grotta Gigante 42c, Sgonico, Trieste 34010, Italy

Corresponding author: Weitao Sun, Jing Ba

Key words: frequency-dependent permeability; Maxwell fluid; rocks; random pore network.

Key Points:

- We study how fluid rheology and pore connectivity affect the permeability of pore networks.
- Fluid rheology has a significant effect on permeability. Peaks are observed on permeability-frequency curves for a Maxwell fluid.
- Pore-network connectivity plays a key role, since the pore radius and mean coordination number lead to permeability variations for the same porosity.

[*] Email: sunwt@tsinghua.edu.cn
[†] Email: jba@hhu.edu.cn

Abstract

Permeability is an important rock property in exploration geophysics. Darcy's law assumes a steady-state regime and constant permeability. However, recent studies showed that the effects of fluid viscosity and pore geometry on permeability cannot be neglected. We consider a Maxwell fluid in a 3D pore network subject to harmonic oscillations. The network is based on the Voronoi method, which provides a realistic connectivity. The permeability of polyethylene oxide (PEO) and cetylpyridinium chloride and sodium salicylate solution (CPyCl/NaSal) have been simulated. The results show that permeability is constant at frequencies less than several kHz, and rapidly decreases to extremely low values as frequency tends to infinite. In addition, we find that fluid mainly flows in sparse-large pore networks at low frequencies and in dense-small pore networks at high frequencies. The Maxwell fluid shows significant permeability peaks related to the mean coordination number (MCN), indicating that there exists an optimal network connectivity at which fluid flow is maximum. These results have been central to understand how fluid flows in natural reservoir rocks. The permeability variations versus frequency, fluid rheology and pore connectivity, provide key information of reservoir fluid properties and pore network structure. The results indicate that it is questionable whether Darcy static permeability can be applied at high frequencies.

1. Introduction

Permeability is an intrinsic property of rocks, characterizing fluid flow in porous media (Carman, 1956; Darcy, 1856; Hazen, 1892; Whitaker, 1986), and it is a key property in groundwater flow, hydrocarbon production and CO_2 storage activities (Backeberg et al., 2017; Carman, 1956; Darcy, 1856; Hazen, 1892; Jang & Santamarina, 2014; Li et al., 2018; Neuzil, 1986; Qin et al., 2018; Teige et al., 2006; Whitaker, 1986). Empirical and semi-empirical relations exist between permeability and micro-structural properties and rock constituents (Alyamani & Sen, 1993; Carcione et al., 2019; Kenney et al., 1984; Kozeny, 1927; Terzaghi & Peck, 1964). Darcy's law describes the steady-state fluid flow through a macroscale porous system. In this case, permeability is assumed constant as a function of frequency. In a natural rock, the pore space structure is complex, containing a large number of fluid-solid interface discontinuities. Adams and Williamson (1923) suggested that flaws close under pressure in rocks. Walsh (1965) pointed out that spherical pores do not close, even with a very high confining pressure, but cracks close under increased confining pressure. Permeability has a non-linear dependency on pore pressure (Walsh & Brace, 1984). The tortuosity, a commonly used quantity describing the pore connectivity and diffusion path curvature in porous media, changes with pressure. There is a "dynamic pathway" for fluid flow under an oscillating pressure. As a consequence, permeability is expected to depend on frequency.

A theoretical expression of dynamic permeability has been developed based on a tortuosity model in fluid-saturated media (Johnson et al., 1987; Smeulders et al., 1992).

In such a theory, the flow is dominated by viscous forces in the low frequency range, while inertial forces are more important at high frequencies. These works confirmed that this semi-phenomenological model can describe the behavior of elastic waves at the low- and high-frequency limits. For intermediate frequencies, the model provides a reasonable approximation. The lattice Boltzmann method (LBM) has been used to calculate the dynamic permeability of a Newtonian fluid in porous media (Pazdniakou & Adler, 2013). The dynamic response of non-Newtonian fluids in tubes revealed an enhancement of the mean flow rate (De Haro et al., 1996; del Río et al., 1998; Tsiklauri & Beresnev, 2001). The flow of a Maxwell fluid in a bundle of capillary tubes has been analyzed by the method of volume averaging (De Haro et al., 1996).

The standard treatment of dynamic permeability and its frequency dependence assumes a non-deformable material saturated with an incompressible fluid (Charlaix et al., 1988; Johnson et al., 1987; Zhou & Sheng, 1989). In this case, there is no pore pressure wave propagating through the medium (i.e., the Biot slow wave). The fluid flows back and forth in the entire pore space in unison, that is, all fluid particles have the same phase. Biot (1956a; b) formulated the theory of wave propagation in a porous medium filled with a compressible viscous fluid. However, the attenuation is caused by the overall drag force depending on the fluid velocity field relative to that of the skeleton. It has been pointed out that fluid velocity gradients are not considered in Biot theory (Sahay, 2008). Hence, the dynamic permeability equations assumed an incompressible fluid and rigid pores, leading to viscosity-dominated and inertia-dominated regimes separated by the Biot characteristic frequency. If the fluid is compressible or the solid phase is deformable, a fluid pressure wave propagates with transmission/reflection at every branching point, leading to wave interference (Bernabé, 2009a; b; Zamir, 1998; 2000). Actually, the fluid would not move in phase (Zamir, 2000). Fluid-flow waves propagate in deformable tubes, or even in rigid pipes saturated by a compressible fluid. Recent laboratory observations confirmed that the rigid-tube assumption holds for steel tubes containing water and air (Kurzeja et al., 2016), but for silicone tubes filled with air, a wave mode can only be explained in the framework of Bernabé's model (Bernabé, 2009a), including the compressibility of the frame (Kurzeja et al., 2016).

In rocks, fluid flow occurs in pore-crack networks, rather than in a single tube or tube bundle. Networks provide a realistic model to describe the pore space configuration. A 2D network model has been developed to predict a static permeability in sandstones (Seeburger & Nur, 1984). Modeling in sandstone and granite indicated that a network model predicts permeability as a function of confining pressure. On the other hand, Bernabé (2009a) studied the pulsatile flow and the related wave propagation in complex networks. The transport properties of a Newtonian fluid in a steady-state regime have been numerically simulated through regular networks consisting of pipes (Bernabé, 1995). Bernabé (2009a) obtained the hydraulic conductivities and wave dispersion equation in rigid and elastic pipe networks saturated with a Newtonian fluid under periodic oscillations. Moreover, he obtained frequency-dependent hydraulic conductivities in a network with varying pipe length and radius. These works lay a foundation for the prediction of permeability of porous media saturated with complex fluids.

In addition to pore connectivity, the fluid properties play an important role. Experimental measurements of the dynamic permeability reported a rollover from a constant value at low frequencies (0.1 Hz to 1 kHz) to a $1/\omega$ dependence at high frequencies (Charlaix et al., 1988). It is believed that there exists a transition from a viscous flow regime to an inertial one as frequency increases. The permeability due to viscoelastic fluids is frequency-dependent, and evidences have been provided by laboratory data (Castrejon-Pita et al., 2003; Mena et al., 1979). Fluid rheology is a significant property controlling permeability. Oil often exhibits significant non-Newtonian behavior in a natural reservoir. The resistance of shear stress corresponding to porous structure deformation is closely related to fluid elasticity and viscosity. However, the mechanism for viscous dissipation due to the interaction of the complex fluid (Maxwell fluid, etc.) and the matrix remains poorly understood. Several studies have introduced complex fluid effects into the classical Biot theory (De Haro et al., 1996; Tsiklauri, 2002; Tsiklauri & Beresnev, 2001). Cui et al. (2010) stated that the dynamic permeability in non-Newtonian (Maxwell) fluid-saturated porous media depends on the Deborah number, which is a parameter characterizing the viscoelastic behavior of the pore fluid. The real part of the permeability increases at frequencies where the imaginary part changes sign (De Haro et al., 1996).

This study first focuses on fluid flow in a single pipe (as a throat in the network) subject to an oscillating pressure based on Bernabé (2009a). The difference is that a Maxwell fluid is used here, which is modelled as series combination of a dashpot and a spring. This fluid is viscoelastic, i.e., it does not obey the classical Hooke elasticity law and Newton viscosity law, which leads to a distinct permeability behavior. Then, we propose a method to predict the frequency-dependent permeability in a 3D random pore network, which is a realistic model for rocks. The network connectivity is characterized by its mean coordination number. The permeability-frequency curves are obtained for regular and random networks saturated with Newtonian and Maxwell fluids. Then, we study the different dynamic behaviors and frequency-dependent permeability of the two types of fluids. The permeability in this study is not the classical one, i.e., the Darcy permeability in the static state regime, but a dynamic permeability in the context of Biot theory.

2. Maxwell fluid flow in a 3D pore network

First, the frequency-dependent dynamic permeability is obtained under an oscillating pressure. Second, random networks are generated consisting of pipes with complex connectivity based on a Voronoi diagram. Then, we propose a method to calculate permeability.

2.1. Flow in a pore throat

We consider an infinitely long cylindrical pipe with a rigid solid wall, which can be regarded as a throat in the pore-throat connecting system. The pipe is filled with a Maxwell fluid of density ρ_f. Fluid velocity is $\mathbf{v}$ and p is the fluid pressure. The mass conservation equation is

$$\frac{\partial \rho_f}{\partial t} + \nabla \cdot \left(\rho_f \mathbf{v} \right) = 0 , \tag{1}$$

and the equation of motion of the fluid is

$$\nabla \cdot \boldsymbol{\tau} = \rho_f \frac{\partial \mathbf{v}}{\partial t} + \nabla p , \tag{2}$$

where $\boldsymbol{\tau}$ is the stress tensor in the fluid and ∇p is the pressure gradient. The expression of $\boldsymbol{\tau}$ varies for different types of fluid. Here, we adopt the Maxwell constitutive equation:

$$\boldsymbol{\tau} + \lambda \dot{\boldsymbol{\tau}} = \eta \dot{\boldsymbol{\gamma}} = \eta \nabla \mathbf{v} , \tag{3}$$

where $\lambda = \eta / G$ is the relaxation time, G is the shear modulus at high frequencies and η is the fluid viscosity. When G is very large (e.g., 10^{15} Pa), λ becomes very small and equation (3) approaches a Newtonian fluid model.

By taking the divergence on both sides of equation (3) and combining it with equation (2), we obtain the momentum conservation equation:

$$\rho_f \frac{\partial \mathbf{v}}{\partial t} + \nabla p + \lambda \rho_f \frac{\partial^2 \mathbf{v}}{\partial t^2} + \lambda \nabla \dot{p} = G \lambda \Delta \mathbf{v} \cdot \tag{4}$$

Equations (1) and (4) are the governing equations of fluid flow in the pore network. In a cylindrical coordinate system (r, θ, z), the fluid velocity has no angular dependence because of symmetry. The velocity vector is $\mathbf{v} = [u, v]^T$, where $u = u(r, z, t)$ and $v = v(r, z, t)$ are the axial and radial components, respectively.

The compressibility of the fluid is $\alpha = \left(1/\rho_f \right) \partial \rho_f / \partial p$. Equations (1) and (4) can be simplified under the assumption of long wavelengths (Bernabé, 2009a). Assuming that the wave propagates in the z-direction, u, v and p have the form of $u(r, z, t) = U(r) \mathrm{e}^{-\iota\omega(t - z/c)}$, $v(r, z, t) = V(r) e^{-\iota\omega(t - z/c)}$ and $p(r, z, t) = P(r) e^{-\iota\omega(t - z/c)}$, where c is the wave speed and $\iota = \sqrt{-1}$ is the imaginary number. Substituting these expressions into equation (4), we have

$$\begin{cases} \dfrac{\mathrm{d}V}{\mathrm{d}\chi} + \dfrac{V}{\chi} + \dfrac{\iota\omega}{c\psi} U = \dfrac{\iota\omega\alpha}{\psi} P \\ \dfrac{\mathrm{d}^2 U}{\mathrm{d}\chi^2} + \dfrac{1}{\chi} \dfrac{\mathrm{d}U}{\mathrm{d}\chi} + U = \dfrac{1}{c\rho_f} P \\ \dfrac{\mathrm{d}^2 V}{\mathrm{d}\chi^2} + \dfrac{1}{\chi} \dfrac{\mathrm{d}V}{\mathrm{d}\chi} + \left(1 - \dfrac{1}{\chi^2} \right) V = \dfrac{1 - \iota\omega\lambda}{G\lambda\psi} \dfrac{\mathrm{d}P}{\mathrm{d}\chi} \end{cases} , \tag{5}$$

where $\psi=\sqrt{\dfrac{\iota\omega\rho_f+\lambda\omega^2\rho_f}{G\lambda}}, \chi=\psi r$. We solve the system of ordinary differential equations with the boundary condition $U(\psi R)=V(\psi R)=0$ in the long-wave approximation, and derive the following solutions:

$$\begin{cases} U(r)\approx AJ_0(\psi r)+\dfrac{1}{\rho_f c}B \\ V(r)\approx -\dfrac{\iota\omega}{c\psi}AJ_1(\psi r)+\dfrac{B}{2}\dfrac{\iota\omega\left(c^2\alpha\rho_f-1\right)}{\rho_f c^2}r \end{cases}, \tag{6}$$

where A and B are undetermined coefficients, J_0 and J_1 are Bessel functions of zero and first orders, respectively, and $P(r)\approx B$. Under the non-slip boundary condition, i.e., $U(R)=V(R)=0$, we get two equations to solve for A and B. The determinant related to the two equations must be zero for any given ω. The dispersion equation of the flow wave in the pipe is

$$c^2=c_0^2\left(1-\frac{2J_1(\psi R)}{\psi R J_0(\psi R)}\right), \tag{7}$$

where c_0 is the sound speed in the fluid. Meanwhile, we get the expression of $U(r)$, and the relation between B and the pressure gradient is $B=c\cdot\nabla P/\iota\omega$ (Bernabé, 2009a), and thus we get $A=-B/\left(\rho_f c J_0(\psi R)\right)$. Therefore, the flux expression can be derived by integrating the axial velocity component over the pipe section, to obtain

$$Q=\frac{-\pi R^2\nabla P}{\iota\omega\rho_f}\left(\frac{2J_1(\psi R)}{\psi R J_0(\psi R)}-1\right). \tag{8}$$

Then, we consider a pipe with a finite length L, and that the pressures at both ends of the pipe are P_i, P_j. The permeability of a single pipe saturated with the Maxwell fluid is (see Appendix):

$$\kappa(\omega)=\frac{-\eta LQ}{S\left(P_j-P_i\right)}=\frac{\iota\pi R^2\eta L}{S\rho_f c}\left(\frac{P_1\cos(\omega L/c)-P_2}{\sin(\omega L/c)\cdot(P_2-P_1)}\right)\left(\frac{2J_1(\psi R)}{\psi R J_0(\psi R)}-1\right), \tag{9}$$

where S is the cross-section area.

2.2. Pore-network building method

The permeability of a representative element volume (REV) (cube with side length h) is calculated for two types of networks: regular and random networks with simple and complex connectivities.

For simplicity, the regular networks are composed of interconnected and vertical cylindrical pipes with the same length L and radius R. In the cubic REV, the number of network nodes (denoted as m) is equal along the three spatial coordinates, and we have a side length $h=(m-1)L$. The porosity of the pore network is $\phi=V_{pipe}/V_{net}$, where V_{pipe} is the total pore space volume, i.e., the volume of a single pipe multiplied by the number of pipes, V_{net} is the volume of the REV containing network and $V_{net}=h^3$. If the porosity and the side length of the REV are given, the length and radius of each pipe are related, i.e., the radius can be calculated if the length is known according to the definition of porosity. In this model, each pipe corresponds to a throat in the rock, and there are no additional pores.

The network space of actual reservoir rocks often contains complex connections. In order to model the porous structure of a real rock, we consider a random network based on a Voronoi cell filling method in a 3D cubic space.

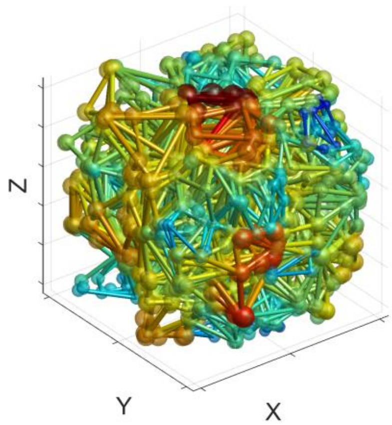

Figure 1. Equivalent random network with pore-throat structure. The color from blue to red indicates a transition from small to large size/radius of the pore/throat.

The pore network consists of two components: spherical pores and cylindrical pore throats. The network reconfiguration consists of three steps: (1) Arrange points randomly in the space, and then take these points as the center of mineral particles (spheres), where the radius of the sphere is taken as a random value according to a rock slice statistical distribution; (2) Take each random point (the center of a sphere) as a reference point, then divide the space into different units by using the 3D Voronoi diagram generation method; (3) Take the vertex of each Voronoi cell as a spherical pore, with the radius of the pore space being proportional to the mean volume of the Voronoi cells near the vertex. The line between vertices is the throat. The pore throat radius is proportional to the cross section area cutting the side. Thus, a 3D pore-throat network is constructed as shown in Figure 1.

The pore-throat network constructed with this method is a simplified equivalent model of the pore structure of a real rock. Although in natural rocks the pore space is highly complex, the fluid flow problem in the pore-throat network model is important because it is amenable to analytical description and it contains much of the physics of the pulsatile wave propagation state.

We analyze the effect of the pore-throat network on permeability. One fundamental parameter to describe the internal pore-throat structure is the mean coordination number (MCN). MCN is the mean connection number to each pore in the network. In 3D regular networks, the MCN of each pore is z = 6. However, in real porous rocks, the MCN has a distribution from 1 to 16 (Øren & Bakke, 2003). In this work, we investigate the behavior of permeability as a function of the MCN. It is straightforward to calculate the MCN when the pore-throat network is constructed. The connections to neighboring pores are summed as coordination numbers and the MCN is obtained by averaging over all the pores.

For each random network, the permeability is determined by solving a set of flux conservation equations at every node. In order to avoid randomness effects of a pore network, the calculation is repeated over 50 network samples. The permeability as a function of the MCN is calculated for different frequencies from 10 Hz to 100 kHz. Interestingly, the significance of the MCN depends on frequency. At low frequency (around 10 Hz), we observe a high permeability in networks with low MCN, i.e., large and sparse pores. At high frequency (from 10 kHz to 100 kHz), high permeability occurs in networks with high MCN, i.e., small and dense pores. The results clearly demonstrate that large and sparse pores with low connectivity dominate the flow at low frequencies. On the contrary, small and dense pores with high connectivity dominate at high frequencies.

2.3. Permeability calculation

In solving a flow problem in a pipe network, the mass conservation at node i will lead to a set of linear equations. The solutions depend on the pressures at related nodes and network connectivity. The frequency-dependent permeability in a given 3D network is obtained numerically based on the following process.

1. If pore i is connected to pore j ($j \in J$) by a pore throat, the flux $Q_i(P_i, P_j)$ at node i is a function of pressures P_i and P_j at node i and j. Here J is a set containing all indices of the pores connected to pore i. In the case of a linear model, we have $Q_i = c_{ij}P_i + d_{ij}P_j$. Here, the coefficients c_{ij}, d_{ij} depend on the throat length and radius (Appendix). For each pore i in the network, the fluid flux at i is conserved, i.e., the sum of the inlet flux equals to the sum of the outlet flux $\sum_{j \in J} Q_i(P_i,\ P_j) = 0$. Every two connected nodes can make up a pipe, and the flux in this pipe is calculated from equation (8). Therefore, the mass conversation equations for each node i yield a set of linear equations which have pore pressures as unknowns,

$$
\begin{cases}
\left(\sum_{j\in J_1} c_{1,j}\right)P_1+\sum_{j\in J_1} d_{1,j}P_j=0\\
\left(\sum_{j\in J_2} c_{2,j}\right)P_2+\sum_{j\in J_2} d_{2,j}P_j=0\\
\vdots\\
\left(\sum_{j\in J_N} c_{N,j}\right)P_N+\sum_{j\in J_N} d_{N,j}P_j=0
\end{cases}, \tag{10}
$$

or briefly $\mathbf{EP}=\mathbf{0}$. For the pores at the inlet and outlet, the pressure values are set as boundary conditions. For pores on surfaces other than the inlet/outlet, periodic boundary conditions are applied.

The coefficient matrix $\mathbf{E}$ described above is obtained as follows. For an arbitrary network, let N and $\mathbf{\Gamma}$ denote the total number of nodes and the connection matrix whose elements are made of 0 or 1, $\mathbf{\Gamma}\in\mathbf{R}^{N\times N}$. The value of the matrix element $\gamma_{ij},\ i,j=1,2,\cdots,N$ is specified according to the connectivity. We have $\gamma_{ij}=1$ if pore i has a connection with pore j, otherwise, $\gamma_{ij}=0$. Nodes are not connected to themselves, i.e., $\gamma_{ii}=0$. It is easy to show that $\mathbf{\Gamma}$ is a symmetric matrix. Consider a microscopic pipe connected by nodes i and j, and that the pressure at these nodes are p_i and p_j. The flux in a single pipe can be rewritten as $Q_i=c_{ij}p_i+d_{ij}p_j$. We introduce the symmetric matrix $\overline{\mathbf{C}}$ and $\overline{\mathbf{D}}$, where $\overline{\mathbf{C}}=\left[c_{ij}\right]_{N\times N},\overline{\mathbf{D}}=\left[d_{ij}\right]_{N\times N}$, and define the two matrices $\mathbf{C}$ and $\mathbf{D}$, where $\mathbf{C}=\mathbf{\Gamma}\otimes\overline{\mathbf{C}}$, $\mathbf{D}=\mathbf{\Gamma}\otimes\overline{\mathbf{D}}$. The matrix operation $\otimes$ is the product of the corresponding elements of two matrices. We can split the coefficient matrix $\mathbf{E}$ into two matrices $\mathbf{E}=\mathbf{E}_1+\mathbf{D}$, where $\mathbf{E}_1=diag\left(\sum_{j=1}^{N}c_{1j},\sum_{j=1}^{N}c_{2j},\cdots,\sum_{j=1}^{N}c_{Nj}\right)$.

2. By solving the linear equations, we get the pressure values at every node. Then the total flux $Q_{total}(\omega)$ of the network from all the inlet pores to the outlet pores are easily calculated by summing all the outlet and inlet pore fluxes. In the form of the Darcy law, the frequency dependent permeability can be calculated by any given pressure difference between inlet and outlet as

$$
\kappa(\omega)=\frac{-\eta h Q_{total}(\omega)}{S\Delta P}, \tag{11}
$$

where h is the REV side length, and ΔP is the pressure difference.

3. Examples

3.1. Influence of fluid type in a regular network

The network is shown in

Figure **2** and its parameters are set as follows: the number of Voronoi cells is 5×5×5, the porosity is 0.1, and the side length of the REV is 1 mm. Then, the length of each micro-tube (pipe) $L = 2.5\times10^{-4}$ m, and the radius of each micro-tube can be calculated from the porosity, giving 2.06×10^{-5} m. The length and radius are consistent with those of Oren (2003) and Okabe (2005). The permeability-frequency relation of the network is shown in Figure 3. The fluid parameters are shown in Table 1 (Sousa et al., 2017; Sung et al., 2003), where water is a Newtonian fluid, and polyethylene oxide (PEO) and cetylpyridinium chloride and sodium salicylate solution (CPyCl/NaSal) are Maxwell fluids.

Table 1. Fluid properties

Fluid	Density (kg/m^3)	Viscosity (Pa·s)	Relaxation time (s)
water	1000	0.001	0
PEO 100 ppm	1104.5	0.0045	1.01×10^{-6}
PEO 500 ppm	1105	0.006	3.9×10^{-6}
CPyCl/NaSal 60 mM	1015	0.7	0.1
CPyCl/NaSal 80 mM	1020	0.5	0.04

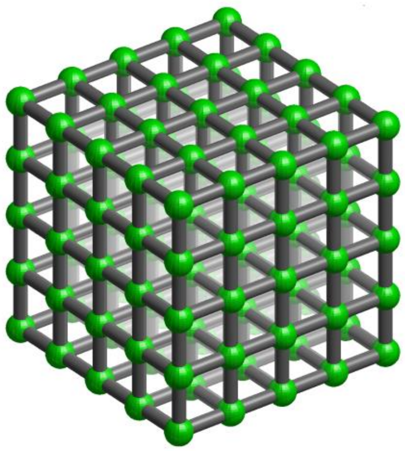

Figure 2. Regular pore network with a 5×5×5 pore configuration.

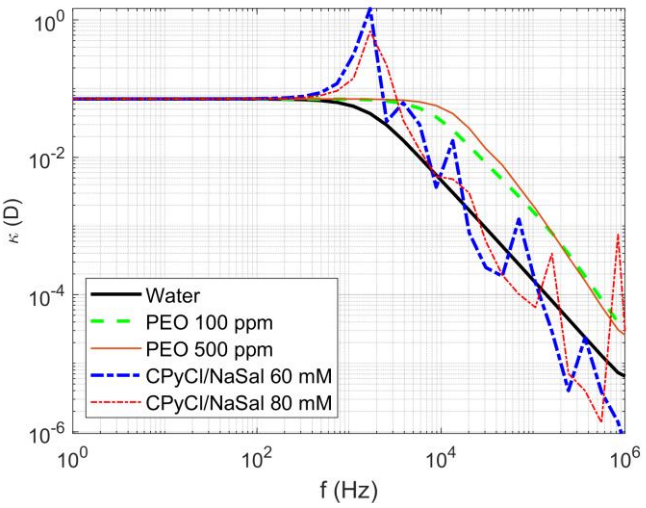

Figure 3. Permeability as a function of frequency for water and Maxwell fluids (PEO and CPyCl/NaSal) in a regular network.

Figure 3 shows that the permeability of the network with Newtonian and Maxwell fluids have the same constant value at low frequencies (approximately 0.07 D below 1 kHz). When the frequency exceeds 1 kHz the permeability decreases. The results for PEO 100 ppm and PEO 500 ppm are basically similar, and follow that of the Newtonian fluid, but show higher values at high frequencies.

The results for CPyCl/NaSal 60 mM and CPyCl/NaSal 80 mM show a downward trend at high frequencies. There are a number of peaks in the permeability curves. The maximum peak value is higher than the steady-state value by more than one order of magnitude. In the case of water and PEO 100 ppm, the viscosity and relaxation time are relatively small and do not show fluctuation peaks. The permeability is constant below 1 kHz.

The differences occur for frequencies higher than 1 kHz, where permeability decreases. These results must be taken into account in wellbore sonic experiments where the frequency may reach 10 kHz. It has been observed in numerical simulations that this permeability decay may shift to lower frequencies when porosity varies. A detailed investigation of this effect will be performed in a future work.

A viscoelastic Maxwell fluid is used, including the frequency-dependent flow enhancement and non-Newtonian effects (del Río et al., 1998; Tsiklauri & Beresnev, 2001). Experiments on viscoelastic fluid dynamics have confirmed the fluctuation peaks under oscillating pressure (Castrejon-Pita et al., 2003). Here, we predict the fluid velocity by a theoretical method and compare it with the experiments. From Equation (6), the axial velocity component is $U(r) \approx AJ_0(\psi r) + B/\rho_f c$, where $A = -B/\left(\rho_f c J_0(\psi R)\right)$ and $B = c \cdot \nabla P/\iota\omega$. The mean velocity is obtained via the integration $\bar{U} = \frac{2}{R^2}\int_0^R rU(r)dr = \frac{\nabla P}{\iota\omega\rho_f}\left(1 - \frac{2J_1(\psi R)}{\psi R J_0(\psi R)}\right)$, where $\psi = \sqrt{\frac{\iota\omega + \lambda\omega^2}{\rho_f \eta}}$.

The fluid parameters are the same as in the experiment (Castrejon-Pita et al., 2003). For CPyCL/NaSal (Maxwell fluid), ρ_f=1050 kg/m^3, η=60 Pa·s, and a relaxation time λ=1.9 s. The pipe radius is 25 mm and the length is 50 cm. The oscillation pressure is created by a piston movement at frequencies between 1.5 and 16 Hz.

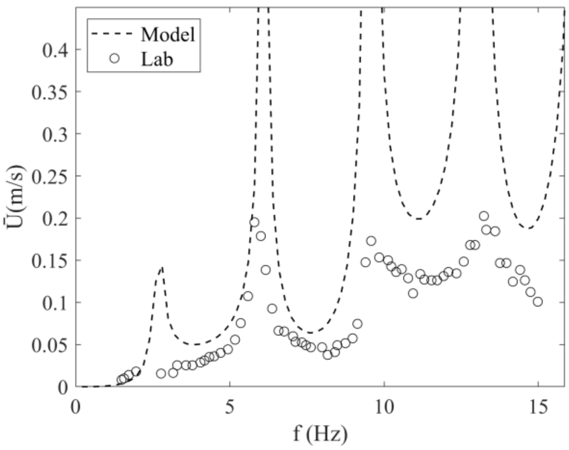

Figure 4. Predicted (dashed line) and experimental (open circles) velocities of CPyCL/NaSal in a transparent cylinder under oscillating pressure at frequencies from 1.5 to 16 Hz. A Maxwell fluid flowing in a pipe under an oscillating pressure is assumed.

Figure 4 shows the predicted and experimentally velocities corresponding to CPyCL/NaSal. Velocity peaks are clearly observed, indicating a resonance mechanism due to the Maxwell fluid. Although the peak heights do not match, their locations are predicted. The dynamic behavior of the Maxwell fluids is quite different from those of water. Such phenomena demonstrate that the influence of the fluid rheology on the permeability cannot be neglected.

3.2. Influence of connectivity in a regular network

Here, we analyze the effects of the network connectivity at constant porosity. There are two ways to get a constant porosity: (1) keep the number of pores fixed and adjust the magnitude of the radius (or the length) of each micro-tube (pipe), which is equivalent to change the size of the REV; (2) keep the size of the REV and adjust the length and radius of each micro-tube, while the porosity can be kept constant by changing the number of pores. The effects of these two choices on the results are examined below.

The fluid properties are given in Table 1. The effect of the size of the REV is investigated first. We choose water as a Newtonian fluid, and PEO 100 ppm and CPyCl/NaSal 60 mM as a Maxwell fluid. The pore configuration is 11×11×11, and the porosity is 0.1. Seven sets of side lengths of the REV are used for the calculation (as shown in Table 2), and the frequencies are 100 Hz and 1 kHz. The relationship between permeability and the radius of each micro tube is shown in **Error! Reference source not found.**, at 100 Hz and 1 kHz. There are seven points on each curve. The abscissa of each point is the radius in Table 2. The results show that permeability increases as the radius increases, because the larger the radius of the micro-tube, the easier the flow.

The three curves overlap when the radius is small, and differ for larger radii. The increase of permeability of the network with water is slower than that of the Maxwell fluids. The increase corresponding to CPyCl/NaSal 60 mM is the fastest one. At 1 kHz, the results of water and PEO 100 ppm show a smooth behavior, but the permeability related to CPyCl/NaSal 60 mM has resonance peaks.

Table 2. Network parameters for different configurations

Porosity	Tube length (mm)	Tube Radius (mm)	REV side length (mm)
	0.2	1.87×10^{-2}	2.0
	0.4	3.74×10^{-2}	4.0
	0.6	5.62×10^{-2}	6.0
0.1	0.8	7.49×10^{-2}	8.0
	1.0	9.36×10^{-2}	10.0
	1.5	1.40×10^{-1}	15.0
	2.0	1.87×10^{-1}	20.0

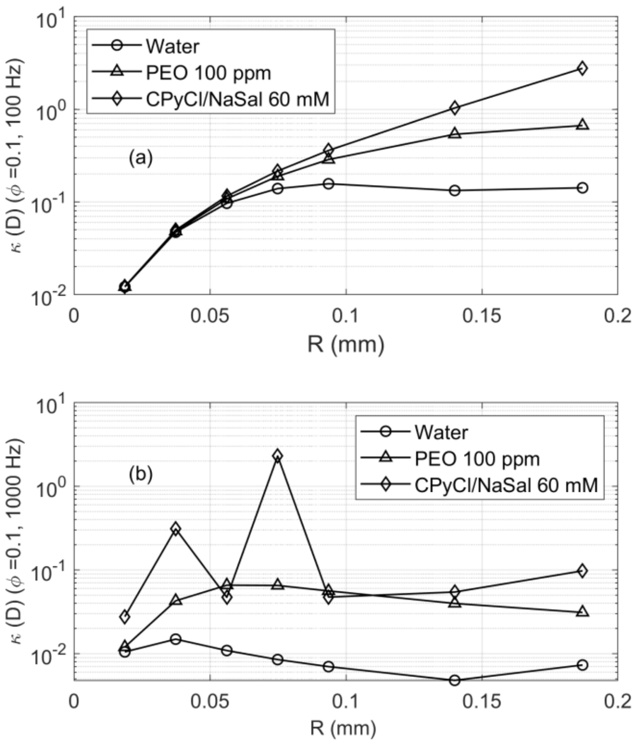

Figure 5. Permeability as a function of the radius of each micro-tube at 100 Hz and 1 kHz.

Next, we investigate the impact of the node configuration of the network on permeability. The side length of the REV is 1 cm, and the porosity is 0.05, 0.1 and 0.2. Seven sets of node configurations are selected for each porosity as shown in Table 3, and we consider frequencies of 100 Hz and 1 kHz.

Table 3. Network parameters for different configurations

Porosity	Tube length (mm)	Tube radius (mm)	REV node configuration
	5.00	0.343	3×3×3
	2.50	0.206	5×5×5
	1.67	0.147	7×7×7
0.1	1.25	0.115	9×9×9
	1.00	0.0937	11×11×11
	0.833	0.0792	13×13×13
	0.714	0.0687	15×15×15

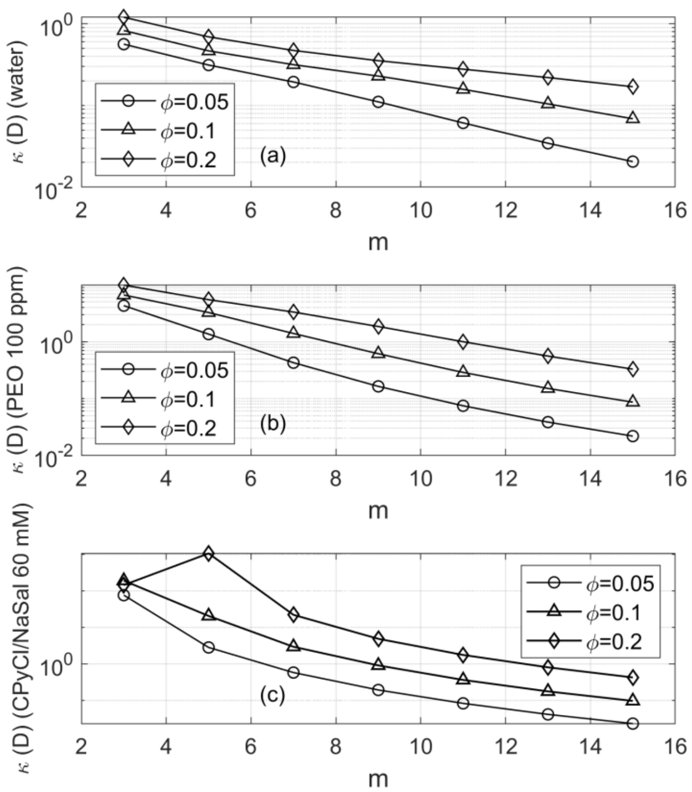

Figure 6. Permeability as a function of grid nodes at 100 Hz. The fluids are (**a**) water, (**b**) PEO 100 ppm, (**c**) CPyCl/NaSal 60 mM

As shown in Figure 6, the pore numbers are the same (denoted as *m*) in each spatial direction, so we take *m* as the abscissa. Figure 6 shows the results for water, PEO 100 ppm and CPyCl/NaSal 60 mM, respectively. As can be seen, permeability depends on the number of nodes, and decreases almost linearly, with different pore-network leading to quite different values.

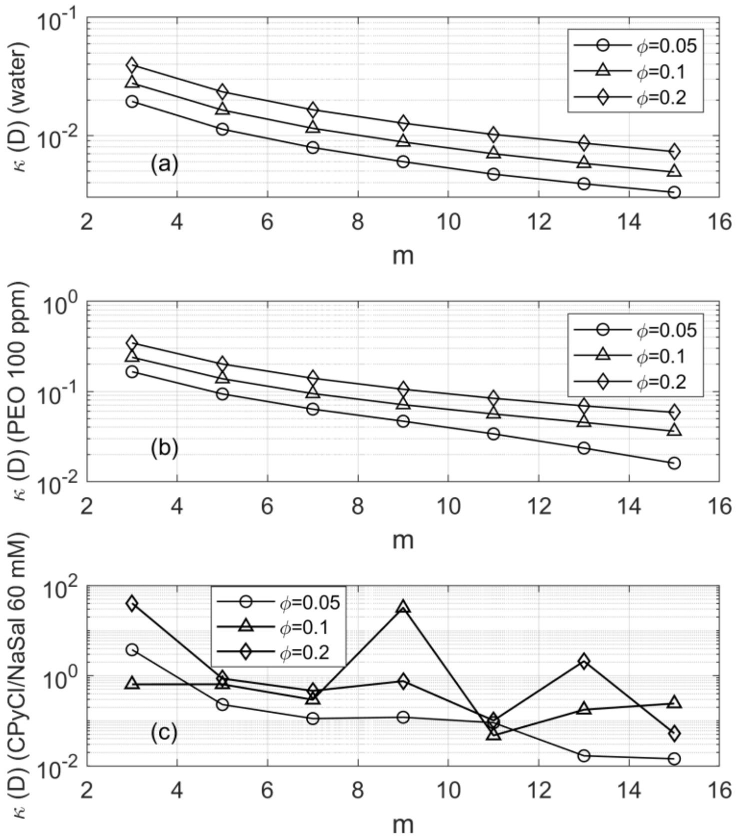

Figure 7. Permeability as a function of grid nodes at 1 kHz. The fluids are (**a**) water, (**b**) PEO 100 ppm, (**c**) CPyCl/NaSal 60 mM.

Figure 7 shows the results at 1 kHz for water, PEO 100 ppm and CPyCl/NaSal 60 mM, respectively. The permeability at 1 kHz is nearly one order of magnitude lower that of 100 Hz. The variation trend is similar for water and PEO 100 ppm. Even if the porosity and the size of the REV are fixed, variations of the pore network configuration greatly affect the permeability. A sparse configuration within the network leads to high permeability. For CPyCl/NaSal 60 mM, peaks can be observed, mainly at 1 kHz.

3.3. Influence of fluid type in a random network

Random pore networks better approximate the internal structure of rocks. We consider a cube with a side length of 1 mm to generate the network. The cubic space is meshed into Voronoi cells with 27- and 216-cell configurations (Figure 8), which are comparable with the lattice networks of size 3×3×3 and 6×6×6. The porosity of the sample, i.e., the volume ratio between pore/pipe network and the overall cube, is set to 0.1. According to the method proposed above, we generate 145 pores for the 27-cell configuration, and 1287 pores for the 216-cell configuration. The pores within a layer (5 % the cubic side) located at x=0 are chosen as the inlet nodes, and a layer at the other side of the cube along the x-direction is the outlet (Figure 8).

We consider water and CPyCl/NaSal 60 mM. The properties are given in Table 1, and the results are shown in Figure 9, where the solid and dashed lines correspond to the

Newtonian (water) and non-Newtonian fluids, respectively. For both types of fluids, the permeability approaches a constant value at low frequency, indicating stationary flow. After exceeding a transition frequency (around 1 kHz), the permeability for water shows an exponential decay. The permeability for the Maxwell fluid also decreases gradually, but with a series of peaks.

For the 216-cell configuration, the number of Voronoi cells filling the cube increases in the process of generating the network, and the permeability differs from that of the 27-cell configuration. The permeability drops to 0.81 Darcy at the steady flow state.

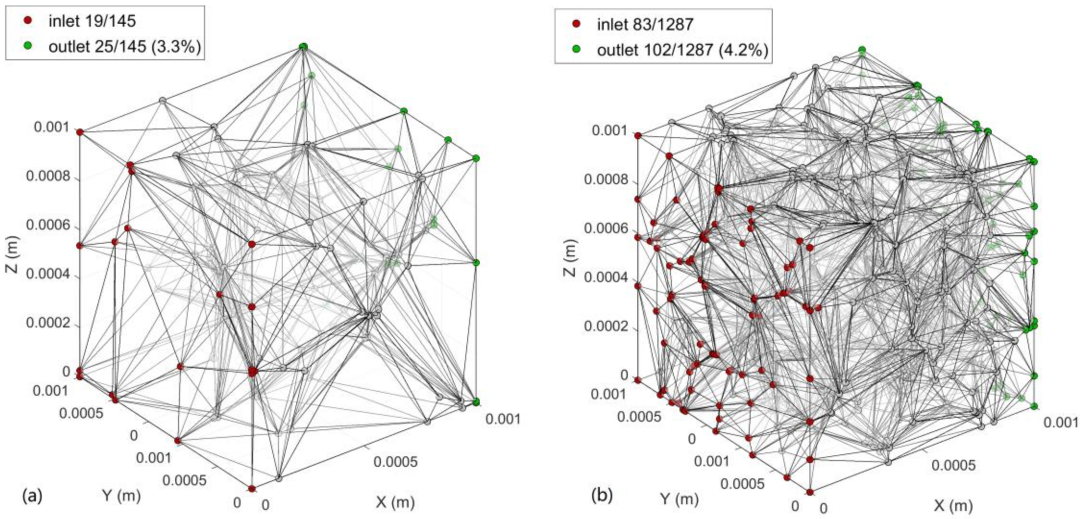

Figure 8. Diagram of the fluid inlet and outlet nodes in the random networks, where (**a**) 27-cell configuration and (**b**) 216-cell configuration.

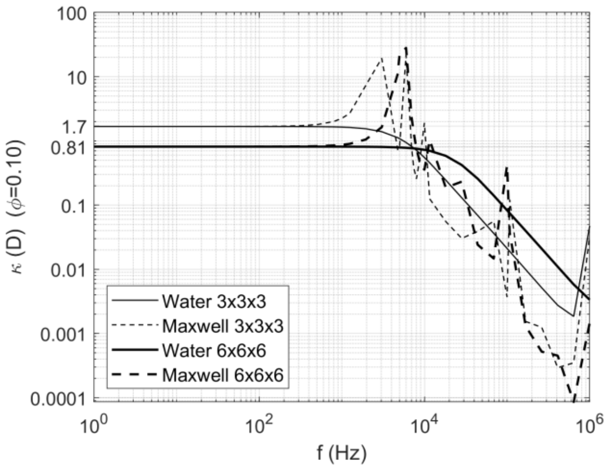

Figure 9. Permeability as a function of frequency for different fluids and pore network configurations.

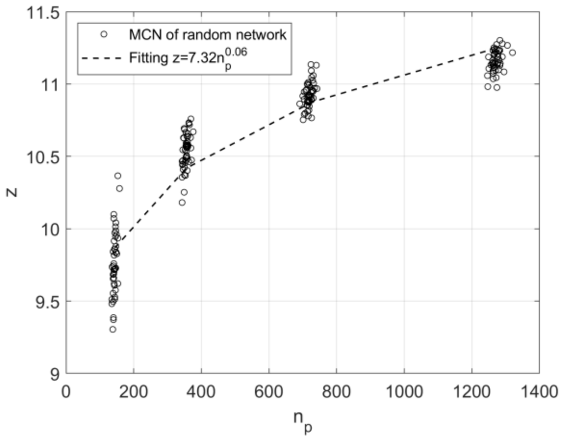

Figure 10. Mean coordination number (MCN) value *z* as a function of the pore number in a random network. Each circle represents the MCN for a single random network. Four types of random networks are created for Voronoi cell numbers 27, 64, 125 and 216, respectively. For each type of network, 50 random network samples are used to reduce the influence of randomness.

We observe that: (1) The frequency-dependent permeability for random pore networks are different for water and Maxwell fluid. The influence of fluid type on permeability cannot be ignored. (2) The pore network structures are quite different for porous media with 27-cell and 216-cell configurations, even if the porosity is the same. Then, the pore size and connectivity significantly affect the permeability.

3.4. Influence of pore connectivity in a random network

Finally, we study the effect of the MCN, which is a direct measure of the pore connectivity. In order to reduce the influence of the randomness of a network, 50 realizations are assumed for each type of network scale. The network scale is measured though the Voronoi cell number. As the cell number increases from 27, 64, 125 to 216, the pore number n_p also increases (see horizontal axis in Figure 10) due to the short pore connectivity in networks with dense pores. For a given porosity, less pores means that the average pore volume is large and pore-pore connections are sparse, i.e., the MCN is small. On the contrary, a large number of pores increases the pore connection density in a unit volume, which leads to a smaller average pore volume and short-path pore-pore connectivity. Thus the MCN is large in such case (Figure 10).

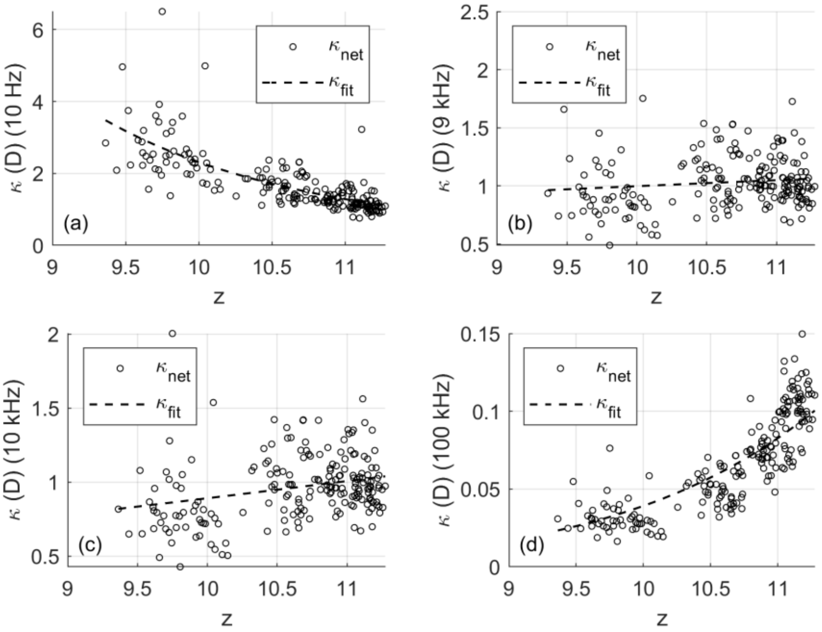

Figure 11. Permeability as a function of MCN (*z* value) at different frequencies for water. The open circles are numerical results and the dashed line is a fitting curve of the power model. (**a**) At low frequencies (10 Hz), permeability decreases as *z* increases from a small value (sparse-large-pore network) to large *z* (dense-small-pore network). (**b**) At intermediate frequencies (9 kHz), permeability is comparable in networks with small and large *z*. (**c**) Permeability in networks with large *z* (dense-small-pore network) becomes prominent as frequency increases. (**d**) At high frequencies (100 kHz), permeability greatly increases in networks with large *z* (dense-small-pore network), but the magnitude is much lower than that at low frequencies.

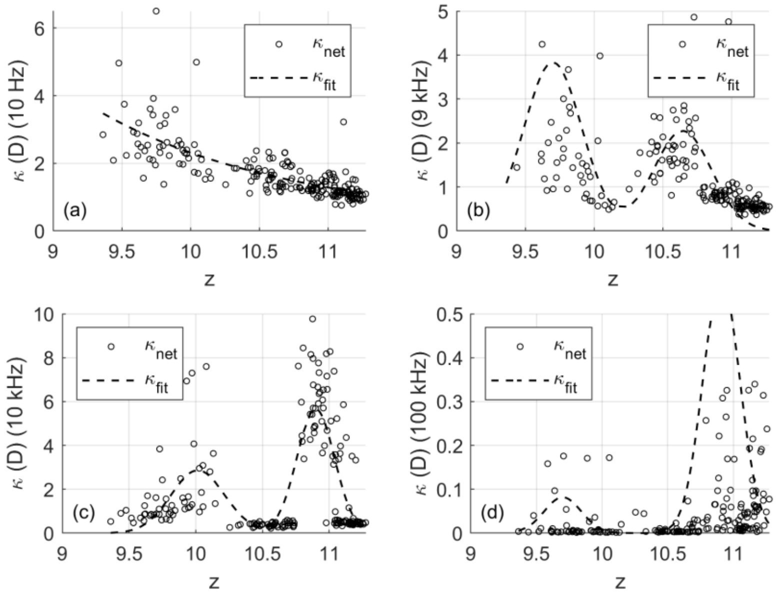

Figure 12. Permeability as a function of MCN (*z* value) at different frequencies for a Maxwell fluid. The open circles are the numerical results and the dashed line is a fitting curve of the power model (for (**a**)) and Gaussian model (for (**b**) to (**d**)). (**a**) At low frequencies (10 Hz), permeability decreases as *z* increases from a small value (sparse-large-pore network) to large *z* (dense-small-pore network). (**b**) At intermediate frequencies (9 kHz), permeability is comparable in networks with small and large *z*. Two peaks appear at MCN around 9.7 and 10.6. (**c**) Permeability in dense-small-pore network (large *z*) exceeds that of the sparse-large-pore network (small *z*) at 10 kHz. (**d**) At high frequencies (100 kHz), the permeability in dense-small-pore network becomes dominant (peak at z=10.9), but the magnitude is much lower than that at low frequencies.

Comparison of the frequency-dependent permeability-MCN relationship for water and CPyCl/NaSal (60 mM) reveals that the sparse-large-pore network (small MCN) dominates at the low frequency limit (Figure 11a) while the dense-small-pore network (large MCN) dominates at the high frequency limit (Figure 11d). At intermediate frequencies (around 9 kHz), the dense-small-pore network has a comparable influence on fluid flow as the sparse-large-pore network (Figure 11c).

The effects of the fluid rheology and pore connectivity are prominent (Figure 12a-d). For a Maxwell fluid, two permeability peaks occur at *z*=9.7 and *z*=10.6 at intermediate frequencies (Figure 12b). As frequency increases from 10 kHz to 100 kHz, the permeability peak related to networks with relatively small and dense pores becomes more important. The results show that for a Maxwell fluid permeability is closely related to the pore network structure (pore size, connectivity, MCN, etc.). At a given frequency, there exists an optimal pore network structure that can enhance the mobility of the pore fluid. For a given pore network structure in natural rocks, there also exists an optimal frequency at which the fluid flows more rapidly. This optimal frequency depends on rock-physics properties such as porosity and fluid rheology. A direct understanding of this observation is that at low frequencies the fluid flows in networks with large and sparse pore/fractures. At high frequencies, the Newtonian flow slows down in sparse-large-pore network, but becomes rapid in dense-small-pore network. For a Maxwell fluid, however, the change in permeability with MCN is even more dramatic. The mechanisms by which these permeability enhancements start to be understood, and many of the important details have yet to be explained.

4. Conclusion

We propose a 3D pore-network generation method based on the Voronoi diagram for random networks, and obtain the frequency-dependent permeability for a Newtonian (water) and Maxwell fluids. The results show that permeability is constant at low frequencies and then decreases rapidly after exceeding a critical frequency. The permeability-frequency curve related to the Maxwell fluid shows resonance peaks. Moreover, the mean coordination number characterizing the connectivity of the pore-network has significant effects on permeability. Fluid flows rapidly in sparse-large-pore network at low frequencies. At the high frequency limit, fluid flow mostly happens in dense-small-pore networks. The present analysis shows the significant effects of fluid rheology and pore connectivity on permeability. The relation between permeability and the micro-structure characteristics provides an approach to quantitatively retrieve the reservoir pore geometry and the connectivity properties from experimental measurements. Further studies should be considered to compare the modeling results with experimental data.

Acknowledgments

The authors are grateful to Yves Bernabé, Maxim Lebedev, and the anonymous reviewer for their valuable suggestions. This study was supported by the National Natural Science Foundation of China (project no. 41874137), the Specially-Appointed Professor Plan of Jiangsu Province, and the Jiangsu Province Innovation and Entrepreneurship Plan of China. The pore structure data associated with Figures 12 and 13 can be accessed at the website (https://zenodo.org/record/3464532).

References

Adams, L. H., and E. D. Williamson (1923), On the compressibility of minerals and rocks at high pressures, *Journal of the Franklin Institute*, *195*(4), 475-529.

Alyamani, M. S., and Z. Sen (1993), Determination of hydraulic conductivity from grain size distribution curves, *Ground Water*, *31*, 551-555.

Backeberg, N. R., F. Iacoviello, M. Rittner, T. M. Mitchell, A. P. Jones, R. Day, J. Wheeler, P. R. Shearing, P. Vermeesch, and A. Striolo (2017), Quantifying the anisotropy and tortuosity of permeable pathways in clay-rich mudstones using models based on X-ray tomography, *Scientific Reports*, *7*(1), 14838, doi:10.1038/s41598-017-14810-1.

Bernabé, Y. (1995), The transport properties of networks of cracks and pores, *Journal of Geophysical Research: Solid Earth*, *100*(B3), 4231-4241, doi:10.1029/94JB02986.

Bernabé, Y. (2009a), Oscillating Flow of a Compressible Fluid through Deformable Pipes and Pipe Networks: Wave Propagation Phenomena, *Pure and Applied Geophysics*, *166*(5), 969-994, doi:10.1007/s00024-009-0484-3.

Bernabé, Y. (2009b), Propagation of Biot slow waves in heterogeneous pipe networks: Effect of the pipe radius distribution on the effective wave velocity and attenuation, *Journal of Geophysical Research: Solid Earth*, *114*(B11), doi:10.1029/2009JB006414.

Biot, M. A. (1956a), Theory of Propagation of Elastic Waves in a Fluid-Saturated Porous Solid .1. Low-Frequency Range, *J Acoust Soc Am*, *28*(2), 168-178, doi:Doi 10.1121/1.1908239.

Biot, M. A. (1956b), Theory of Propagation of Elastic Waves in a Fluid-Saturated Porous Solid .2. Higher Frequency Range, *J Acoust Soc Am*, *28*(2), 179-191, doi:Doi 10.1121/1.1908241.

Carcione, J. M., D. Gei, T. Yu, and J. Ba (2019), Effect of Clay and Mineralogy on Permeability, *Pure and Applied Geophysics*, *176*(6), 2581-2594, doi:10.1007/s00024-019-02117-3.

Carman, P. C. (1956), *Flow of gases through porous media*, Academic press, New York.

Castrejon-Pita, J. R., J. A. del Rio, A. A. Castrejon-Pita, and G. Huelsz (2003), Experimental observation of dramatic differences in the dynamic response of Newtonian and Maxwellian fluids, *Physical review. E, Statistical, nonlinear, and soft matter physics*, *68*(4 Pt 2), 046301, doi:10.1103/PhysRevE.68.046301.

Charlaix, E., A. P. Kushnick, and J. P. Stokes (1988), Experimental Study of Dynamic Permeability in Porous Media, *Physical Review Letters*, *61*(14), 1595-1598.

Cui, Z. W., J. X. Liu, G. J. Yao, and K. X. Wang (2010), Borehole guided waves in a non-Newtonian (Maxwell) fluid-saturated porous medium, *Chinese Phys B*, *19*(8).

Darcy, H. (1856), Les fontaines publiques de la ville de Dijon*Rep.*, Paris: Dalmont.

De Haro, M. L., J. A. P. Del Río, and S. Whitaker (1996), Flow of Maxwell fluids in porous media, *Transport in Porous Media*, *25*(2), 167-192, doi:10.1007/BF00135854.

del Río, J. A., M. López de Haro, and S. Whitaker (1998), Enhancement in the dynamic response of a viscoelastic fluid flowing in a tube, *Physical Review E*, *58*(5), 6323-6327.

Hazen, A. (1892), Some physical properties of sands and gravels, with special reference to their use in filtration*Rep.*, 539–556 pp.

Jang, J., and J. C. Santamarina (2014), Evolution of gas saturation and relative permeability during gas production from hydrate-bearing sediments: Gas invasion vs. gas nucleation, *Journal of Geophysical Research: Solid Earth*, *119*(1), 116-126, doi:10.1002/2013JB010480.

Johnson, D. L., J. Koplik, and R. Dashen (1987), Theory of dynamic permeability and tortuosity in fluid-saturated porous media, *Journal of Fluid Mechanics*, *176*, 379-402, doi:10.1017/S0022112087000727.

Kenney, T. C., D. Lau, and G. I. Ofoegbu (1984), Permeability of compacted granular materials, *Canadian Geotechnical Journal*, *21*, 726-729.

Kozeny, J. (1927), Uber kapillare leitung des wassers im boden, *Sitzungsber Akad. Wiss., Wien,*, *136*(2a), 271-306.

Kurzeja, P., H. Steeb, M. A. Strutz, and J. Renner (2016), Oscillatory fluid flow in deformable tubes: Implications for pore-scale hydromechanics from comparing experimental observations with theoretical predictions, *The Journal of the Acoustical Society of America*, *140*(6), 4378-4395, doi:10.1121/1.4971365.

Li, S., C. Qiao, Z. Li, and Y. Hui (2018), The effect of permeability on supercritical CO2 diffusion coefficient and determination of diffusive tortuosity of porous media under reservoir conditions, *Journal of CO2 Utilization*, *28*, 1-14.

Mena, B., O. Manero, and D. M. Binding (1979), Complex flow of viscoelastic fluids through oscillating pipes. Interesting effects and applications, *Journal of Non-Newtonian Fluid Mechanics*, *5*, 427-448.

Neuzil, C. (1986), Groundwater Flow in Low-Permeability Environments, *Water Resources Research* *22*(8), 1163-1195.

Okabe, H., and M. J. Blunt (2005), Pore space reconstruction using multiple-point statistics, *Journal of Petroleum Science and Engineering*, *46*(1-2), 121-137.

Øren, P. E., and S. Bakke (2003), Reconstruction of Berea sandstone and pore-scale modelling of wettability effects, *Journal of Petroleum Science and Engineering*, *39*(3-4), Journal of Petroleum Science and Engineering.

Pazdniakou, A., and P. M. Adler (2013), Dynamic permeability of porous media by the lattice Boltzmann method, *Advances in Water Resources*, *62*, 292-302.

Qin, Y., Y. Wu, P. Liu, F. Zhao, and Z. Yuan (2018), Experimental studies on effects of temperature on oil and water relative permeability in heavy-oil reservoirs, *Scientific Reports*, *8*(1), 12530, doi:10.1038/s41598-018-31044-x.

Sahay, P. N. (2008), On the Biot slow S-wave, *GEOPHYSICS*, *73*(4), N19–N33.

Seeburger, D. A., and A. Nur (1984), A pore space model for rock permeability and bulk modulus, *Journal of Geophysical Research: Solid Earth*, *89*(B1), 527-536, doi:10.1029/JB089iB01p00527.

Smeulders, D. M. J., R. L. G. M. Eggels, and M. E. H. van Dongen (1992), Dynamic permeability: reformulation of theory and new experimental and numerical data, *Journal of Fluid Mechanics*, *245*, 211-227, doi:10.1017/S0022112092000429.

Sousa, P. C., E. J. Vega, R. G. Sousa, J. M. Montanero, and M. A. Alves (2017), Measurement of relaxation times in extensional flow of weakly viscoelastic polymer solutions, *Rheologica Acta*, *56*(1), 11-20, doi:10.1007/s00397-016-0980-1.

Sung, K., M. S. Han, and C. Kim (2003), Rheological behavior and wall slip of dilute and semidilute CPyCl/NaSal surfactant solutions, *Korea Australia Rheology Journal*, *15*(3), 151-156.

Teige, G. M. G., W. L. H. Thomas, C. Hermanrud, P.-E. Øren, L. Rennan, O. B. Wilson, and H. M. Nordgård Bolås (2006), Relative permeability to wetting-phase water in oil reservoirs, *Journal of Geophysical Research: Solid Earth*, *111*(B12), doi:10.1029/2005JB003804.

Terzaghi, K., and R. B. Peck (1964), *Soil Mechanics in Engineering Practice*, John Wiley and Son, New York.

Tsiklauri, D. (2002), Phenomenological model of propagation of the elastic waves in a fluid-saturated porous solid with nonzero boundary slip velocity, *The Journal of the Acoustical Society of America*, *112*(3), 843-849.

Tsiklauri, D., and I. Beresnev (2001), Enhancement in the dynamic response of a viscoelastic fluid flowing through a longitudinally vibrating tube, *Physical Review E*, *63*(4), 046304.

Walsh, J. B. (1965), The effect of cracks on the compressibility of rock, *Journal of Geophysical Research (1896-1977)*, *70*(2), 381-389, doi:10.1029/JZ070i002p00381.

Walsh, J. B., and W. F. Brace (1984), The effect of pressure on porosity and the transport properties of rock, *Journal of Geophysical Research: Solid Earth*, *89*(B11), 9425-9431, doi:10.1029/JB089iB11p09425.

Whitaker, S. (1986), Flow in porous media I: A theoretical derivation of Darcy's law, *Transport in Porous Media*, *1*(1), 3-25.

Zamir, M. (1998), Mechanics of blood supply to the heart: wave reflection effects in a right coronary artery, *Proceedings of the Royal Society of London. Series B: Biological Sciences*, *265*(1394), 439-444, doi:10.1098/rspb.1998.0314.

Zamir, M. (2000), *The Physics of Pulsatile Flow*, Springer, New York.

Zhou, M.-Y., and P. Sheng (1989), First-principles calculations of dynamic permeability in porous media, *PHYSICAL REVIEW B*, *39*(16), 12027-12039.

Appendix

Let us consider a pipe of length *L*, that the pressure at both ends are P_i, P_j, and the fluxes are Q_i, Q_j. The total pressure in the pipe is the superposition of two plane waves propagating in opposite directions (Bernabé, 2009a):

$$p(z,t) = B^{+}\mathrm{e}^{-\iota\omega(t-z/c)} + B^{-}\mathrm{e}^{-\iota\omega(t+z/c)}, \qquad \text{(A1)}$$

where $\iota = \sqrt{-1}$ is the imaginary unit. In order to satisfy the initial and boundary conditions $p(0,0)=P_i$, $p(L,0)=P_j$, we obtain

$$B^{+} = \frac{P_j - P_i\mathrm{e}^{-\iota\omega L/c}}{\mathrm{e}^{\iota\omega L/c} - \mathrm{e}^{-\iota\omega L/c}}, \quad B^{-} = \frac{P_i\mathrm{e}^{-\iota\omega L/c} - P_j}{\mathrm{e}^{\iota\omega L/c} - \mathrm{e}^{-\iota\omega L/c}}, \qquad \text{(A2)}$$

In the same manner, the total flow in the pipe is

$$q(z,t) = Q^{+}\mathrm{e}^{-\iota\omega(t-z/c)} + Q^{-}\mathrm{e}^{-\iota\omega(t+z/c)}, \qquad \text{(A3)}$$

The fluxes at both ends differ, i.e., $Q_i = Q^{+} + Q^{-}$ and $Q_j = Q^{+}e^{\iota\omega L/c} + Q^{-}e^{-\iota\omega L/c}$ are not the same, forming a storage inside the pipe. If there are no sources or sinks at node i, the flow is conserved at this node. If pore i is connected to pore j by a throat, the flux from i to j can be defined as the positive direction, without loss of generality. Regarding the flow from node i to node j ($j \in J$) by multiple pore throats, where J is a set containing all indices of the nodes connected to node i, we consider the flow conservation at node i $\sum_{j\in J} Q_i(P_i,\ P_j) = 0$. The flux at node i is

$$Q_i = \frac{-\iota\pi R_{ij}^2}{\rho_f c}\left(\frac{P_i\cos(\omega L_{ij}/c) - P_j}{\sin(\omega L_{ij}/c)}\right)\left(\frac{2J_1(\psi R_{ij})}{\psi R_{ij} J_0(\psi R_{ij})} - 1\right), \qquad \text{(A4)}$$

where L_{ij} and R_{ij} are the length and radii of the pipe, respectively. From equation (A4), we have that the flux Q_i is a combination of pressure P_i and P_j

$$Q_i = c_{ij} p_i + d_{ij} p_j , \tag{A5}$$

where $c_{ij} = \frac{-\iota\pi R_{ij}^2}{\rho c_0} \frac{\cos(\omega L_{ij}/c_0)}{\sin(\omega L_{ij}/c_0)} \left(\frac{2J_1(\psi R_{ij})}{\psi R_{ij} J_0(\psi R_{ij})} - 1 \right)$ and $d_{ij} = \frac{\iota\pi R_{ij}^2}{\rho c_0} \frac{1}{\sin(\omega L_{ij}/c_0)} \left(\frac{2J_1(\psi R_{ij})}{\psi R_{ij} J_0(\psi R_{ij})} - 1 \right)$.

Knowing the flux Q over a pipe of length *L* and cross-sectional area *S*, as well as the pressure difference, the permeability can be derived as $\kappa = -\eta LQ / S(P_j - P_i)$ by simply rearranging Darcy's law. In the case of negligible intrinsic flux storage in a throat, the permeability with a single throat saturated by the Maxwell fluid is

$$\kappa(\omega) = \frac{-\eta LQ}{S(P_j - P_i)} = \frac{\iota\pi R^2 \eta L}{S\rho_f c} \left(\frac{P_i \cos(\omega L/c) - P_j}{\sin(\omega L/c) \cdot (P_j - P_i)} \right) \left(\frac{2J_1(\psi R)}{\psi R J_0(\psi R)} - 1 \right). \tag{A6}$$